Laser Interferometric Measurements of a Laser-Preionization-Triggered Spark Column

WAYNE D. KIMURA, MEMBER, IEEE, MARK J. KUSHNER, MEMBER, IEEE, E. A. CRAWFORD, AND S. R. BYRON

Abstract—**A KrF laser (248 nm) is used to volume preionization trigger a 40–100-kV, > 10-kA, 100-ns spark gap switch. This method of triggering creates reproducible and axisymmetric spark columns having low temporal and spatial jitter. A short pulse (< 5 ns) tunable dye laser and a Mach–Zehnder interferometer are used to obtain spatial and temporal measurements of the spark column. The spatial resolution of the interferograms is better than 5 μm. The fringe shifts of the interferograms are used to calculate the electron and heavy particle density distributions within the spark column as a function of time during the spark. Results are presented for sparks in 5-percent SF_6/20-percent N_2/75-percent He and 1-percent Xe/99-percent H_2 gas mixtures. Dc and pulsed self-breakdown voltages are also measured in order to provide a reference for the laser-triggered results. Data on laser-triggering reliability and spark breakdown delay time are also presented.**

I. INTRODUCTION

SPARK GAP switches are critical components in many high-power devices such as lasers and particle accelerators [1]. Although spark gap switches are commonly used, there are still many aspects of their operation that are not well understood, some of which are closure time, electrical loss, recovery, and lifetime. A well-established understanding of these characteristics will result in better switch designs, thereby greatly improving the performance of devices using spark gap switches. Past advances in switch technology have been based primarily upon empirical methods, resulting in part from the lack of detailed understanding of basic spark column physics and the lack of experimental data required to verify models of the spark formation.

The goal of the work discussed in this paper is to devise methods of improving closing switch technology by first increasing our understanding of spark column formation physics. The experiment features the use of a laser interferometric diagnostic system capable of recording the development of a laser-preionization-triggered 100-ns, 40–100-kV, > 10-kA spark channel with a spatial and temporal resolution of 5 μm and 5 ns, respectively. The experiment also uses calibrated current and voltage measurement techniques in order to obtain direct and reliable experimental data on energy dissipation in spark switches.

Using interferometers to examine dense plasma is not new, although recent interest has been mostly with plasmas and spark channels associated with the plasma fusion effort [2], [3]. In the work reported here, we combine laser preionization triggering with laser interferometry to obtain highly reproducible spark columns in a switch device whose characteristics are typical of those in high-power spark gap switches. As will be shown, the laser preionizes the gas between the switch electrodes to initiate spark breakdown. The method does not rely on the laser beam striking an electrode as is done in many other laser-triggering schemes [4], [5].

Laser preionization triggering (hereafter referred to simply as laser triggering) of spark gaps provides two advantages. First, the start of the spark breakdown and the position of the spark can be controlled very accurately by the trigger laser. This ability to control the spark initiation and location enables accurate temporal and spatial measurements with the laser interferometer. The second advantage is that under appropriate switch conditions laser triggering generates reproducible axisymmetric spark channels, virtually eliminating the role and the effects of axial streamer propagation [6]. This symmetry greatly simplifies the task of understanding the spark column pattern produced by the interferometer.

This study did not examine the effects of electrode shape or composition on the spark column formation. There are indications that the spark column attaches to the edge of the holes in the electrodes through which the trigger-laser beam enters and exits. During the self-break measurements, which will be discussed later in this paper, the spark column tends to form randomly over a broader area of the electrode. We believe the method of laser triggering used in this work is less sensitive to electrode effects than when the laser strikes the electrode.

The light source for the interferometer is a tunable short pulse (< 5 ns) dye laser. This permits "snapshots" of the spark column to be taken at various times during its evolution and at various wavelengths. From these interferograms the electron and heavy particle density profiles within the column can be determined. Data obtained from these measurements are used to verify a computer model of spark channel formation. This model and its comparison with the experimental data are discussed in detail elsewhere [7].

The experimental setup is described in Section II. In Section III, self-breakdown measurements are discussed;

Manuscript received August 26, 1985; revised February 18, 1986. This work was supported by the Naval Surface Weapons Center under Contract N60921-83-A057.

The authors are with Spectra Technology, Inc., Bellevue, WA 98004.

IEEE Log Number 8608390.

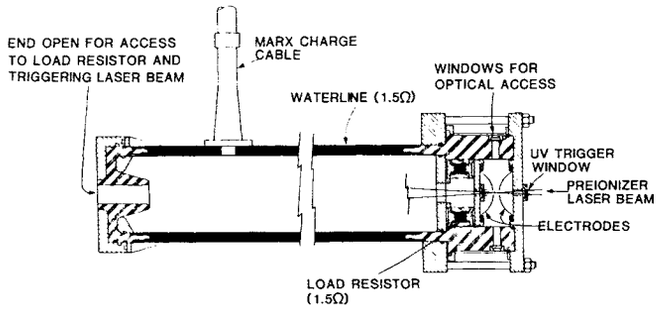

Fig. 1. Cross-sectional view of waterline PFL, liquid load resistor, and spark gap chamber. The electrodes are copper hemispheres with a 7-cm radius and a 1-mm-diameter hole in their center. The outer diameter of the spark chamber is 27 cm.

these data are used to provide a reference for the laser-triggered results. Examples of interferometric measurements of the spark column are given in Section IV for both laser-triggered and self-breaking arcs. The reliability of our laser-triggering system is discussed in Section V. Section VI describes how the data from the experiment are analyzed and presents typical results. Concluding remarks are given in Section VII.

II. Description of Experiment

The basic components of the experiment consist of an electrical and an optical system. The electrical components include a pulse power system which charges a pulse-forming line (PFL) attached to a specially designed spark chamber housing a load resistor and the spark gap electrodes. The optical part of the system consists of an excimer laser and optical delivery system for triggering the spark gap, and a dye laser/interferometer diagnostic system for examining the spark column. These components are described below.

A two-stage Marx bank [8] charges the water dielectric PFL to 40–100 kV in a time period of 1.8 μs with a design efficiency of nearly 100 percent. The PFL has a capacitance of 40 nF and the Marx bank has an erected capacitance of 40 nF; hence, when the voltage on the PFL reaches a maximum, the remaining voltage and charge on the charging Marx is nearly zero. If the line is discharged at peak voltage, then the current to the load is due to the line current only.

The PFL is 1.7 m long (corresponding to a 100-ns pulse duration) and is designed for an impedance of 1.5 Ω when operated with a water dielectric. Fig. 1 shows a cross-sectional view of the waterline PFL connected to the spark gap chamber. Water is continuously circulated from the line through a deionizer column, a reservoir, and is returned to the line. The line has a hollow interior that allows access to the preionizer laser beam. This beam exits through the hole in the large insulator at the open circuit end of the line, and may be observed on a fluorescent screen to facilitate alignment of the beam. The hollow line also provides access for circulation of fluid to the liquid load resistor. When saturated $CuSO_4$ solution is used, the load resistor is designed to have a resistance of 1.5 Ω

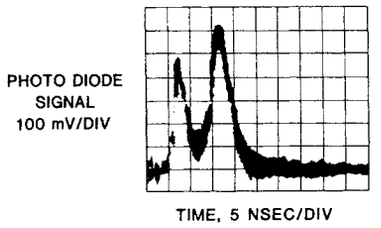

Fig. 2. Oscilloscope record showing time history of the KrF preionization laser output. The record is an overlay of 20 shots. The double-pulse output is caused by the PFN of the particular laser used and is not typical of commercial discharge excimer lasers.

to match the line impedance. The load resistor is also hollow to permit the egress of the preionizer beam.

The preionizer beam enters and exits the chamber through fused silica windows oriented perpendicular to the longitudinal axis of the PFL. The beam passes through 1-mm-diameter holes centered in the hemispherical copper discharge electrodes (7-cm radius). Also present in the discharge chamber are four ports oriented 90° apart azimuthally and located on the midplane between the electrodes. The ports allow 2.2 cm of clear aperture for optical observation. Two of the ports are used as windows for optical access by the interferometer probe beam.

A commercial discharge excimer laser (Exci-lite™ Model 401) is used as the spark preionization source. All experiments were performed with this device operating as a KrF laser (248 nm). To obtain minimum beam divergence, the laser is equipped with an unstable oscillator cavity consisting of a 1-m-radius spherical mirror and a 25-cm-radius dot output coupler.

The temporal history of the laser output was measured using a fast Hamamatsu photodiode and a Tektronix 7104 oscilloscope having a > 400-MHz bandwidth. A typical oscilloscope record is given in Fig. 2. It shows that the laser output consists of a very short duration pulse, approximately 2.5 ns long (FWHM), followed 10 ns later by a larger pulse of 5-ns FWHM duration. The double pulsing is caused by ringing of the pulse-forming network (PFN) in this particular laser; it is not typical for commercial discharge lasers. The laser output and temporal history is quite reproducible shot to shot. The double-pulse output from the preionizer laser does not appear to affect its performance since spark breakdown typically starts immediately after the arrival of the first pulse. The beam divergence is about 0.2 mrad (FWHM) or about two times the diffraction limit.

Fig. 3 is a plan view of the spark channel interferometer system. The output from the preionizer KrF laser is guided with a pair of mirrors to an 18-cm lens which focuses the laser beam into the spark chamber through a window at the end of the PFL. The focus is centered between the electrodes. This focusing arrangement can be modified to permit simultaneous laser triggering of multiple spark channels [9]. The separation between the electrodes is 1.2 cm, and this was kept constant during all the experiments.

A second Exci-lite KrF laser is used to pump the dye laser. The dye laser emits a single < 5-ns duration pulse.

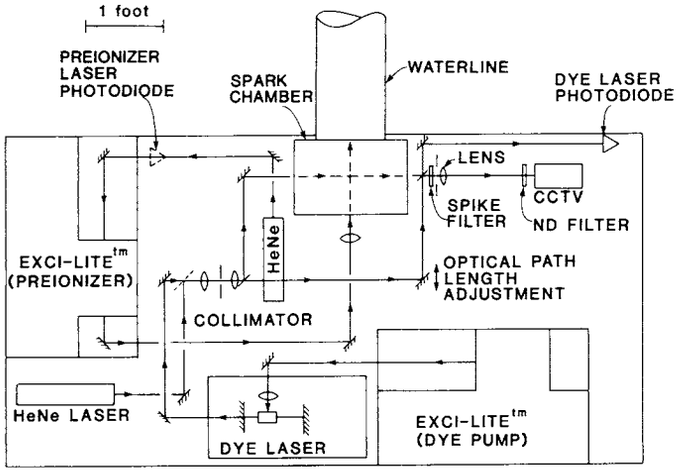

Fig. 3. Plan view of the laser-triggering and interferometer diagnostic system used during the experiments.

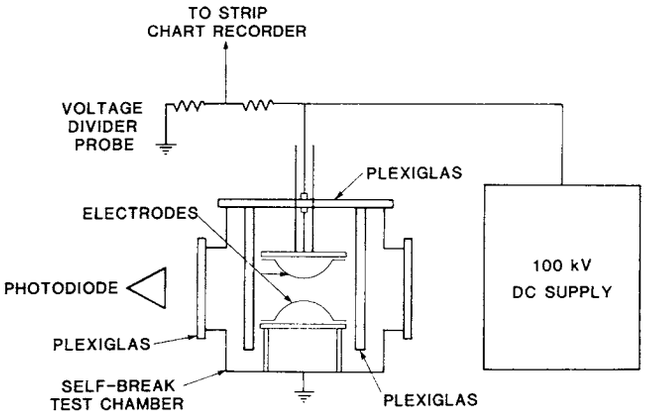

Fig. 4. Schematic of the off-line dc self-breakdown spark test chamber.

The dye laser output passes through a collimator before entering into a Mach–Zehnder interferometer. One branch of the interferometer passes through the spark channel. A lens at the output of the interferometer images the spark column onto a vidicon camera. Through appropriate selection of lenses and focal distances, the spark column can be examined from 1*X* to 18*X* magnification. A spike (bandpass) filter and neutral density filters are positioned in front of the camera to eliminate the broad-band emission from the spark while permitting detection of the dye laser beam.

The preionizer laser is fired via a fiducial signal originating from within the Marx system. The dye laser is fired at various delay times after the preionizer triggers the spark gap. This allows probing of the spark channel at various times during the spark history. The timing of the two lasers is verified by intercepting a small amount of the stray light produced by the two lasers and recording the signals with a fast photodiode. All electrical lengths, optical paths, and cable delays are correlated to within 2 ns and the estimated cable rise-time response is 1 ns.

Current through the spark column is measured using a current viewing resistor (CVR). It consists of a 0.013-mm (0.0005 in) Inconel foil which forms the coaxial (27 cm diameter) current return for the switch. The CVR was calibrated *in situ* with a known current source.[1]

A specially designed capacitive voltage divider probe [10] is used to measure the voltage drop across the spark gap. This probe is housed inside the spark chamber and has a response time of < 1 ns. The voltage and current probes together with the interferograms permit detailed measurements of the arc resistance as discussed in [11].

III. Self-Breakdown Measurements

The fraction of self-breakdown voltage F_{SB} for a number of gas mixtures and conditions was measured separately from the primary experiments. Although pulsed self-breakdown measurements can be obtained using the waterline PFL system, such measurements risk damaging the waterline. When the spark chamber switch does not self-break, breakdown and arcing may occur within the waterline, resulting in damage that cannot be easily repaired. In addition, the waterline cannot be dc charged and therefore cannot yield true dc values of F_{SB}.

In order to obtain the functional dependence of F_{SB} for our conditions, a separate test chamber was built and is sketched in Fig. 4. The chamber contains an identical set of electrodes as used in the laser-triggered spark gap and has the same electrode spacing (1.2 cm). A capacitor in parallel with the electrodes is quasi-dc charged (charging time is approximately 2 s) with a dc power supply connected to the capacitor through a large resistive load. A resistive voltage divider monitors the voltage on the electrodes with the output displayed on a strip chart recorder. Breakdown is indicated by the rapid collapse of the voltage recorded by the resistive voltage divider. Statistical data are obtained by letting the device operate open loop; that is, allowing the dc power supply to continually charge the capacitor. The charging time is sufficiently long, and the energy dissipated in the spark column sufficiently small, that total recovery of the spark gap is obtained. Typical standard deviations for the self-breakdown voltages ranged from 0.1 to 1 kV.

For all the gas mixtures measured, the dc self-breakdown voltage is a linear function of gas pressure. Examples of dc self-breakdown voltages measured in the test chamber are plotted in Fig. 5. Assuming linearity, the dc self-breakdown voltage V_{SB} can be obtained from the expression

$$V_{SB} = C_{SB} \cdot Pd$$

where C_{SB} is the self-breakdown coefficient having units of kV $\cdot$ atm^{-1} $\cdot$ cm^{-1}, P is the gas pressure in atmosphere, and d is the electrode spacing in centimeters. The values measured for C_{SB} from this work are listed in Table I.

Also plotted in Fig. 5 as the open symbols for SF_6 and 30-percent SF_6/70-percent N_2 are pulsed self-breakdown

[1]A dc measurement of the resistance of the foil (made on a sample of the material) showed a nominal sensitivity of 0.138 kA/V. The calibration was checked by direct application of dc current to the CVR and was found to be 0.135 kA/V. The slight difference is due to extra resistance in the foil because of small cutouts in the foil for the optical ports.

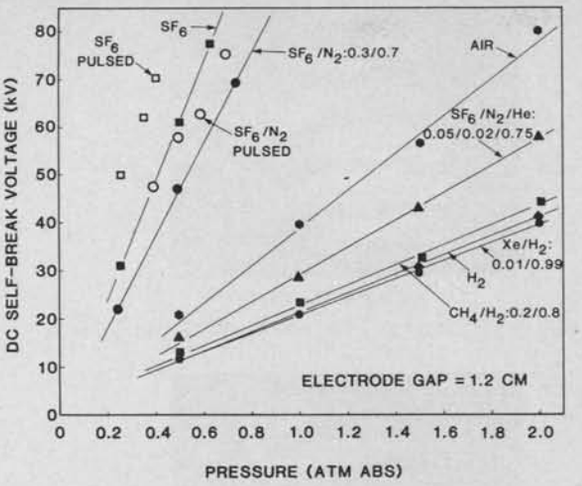

Fig. 5. Dc and pulsed (open symbols) self-break voltages for various gas mixtures.

TABLE I
DC SELF-BREAKDOWN VOLTAGE COEFFICIENTS (C_{SB})

Gas Mixture	C_{SB} (kV atm^{-1} cm^{-1})
1% Xe/99% H_2	16.7
H_2	17.4
20% CH_4/80% H_2	18.2
5% SF_6/20% N_2/75% He	25.0
Dry Air	32.4
30% SF_6/70% N_2	76.9
SF_6	108.3

data. These data were obtained on the 1.5-Ω waterline (charging time 1.8 μs). Only a few data points were taken to minimize the risk of damaging the waterline. The pulsed self-breakdown voltages for our geometry are approximately 10–20 percent higher than those for the dc self-breakdown voltage having otherwise identical conditions.

In this paper, data obtained for a particular gas mixture and pressure are referenced either to the peak voltage just before the onset of voltage collapse V_{peak} or to F_{SB}. It is possible to correlate F_{SB} with E/N (electric field/gas number density) by using Fig. 5.

Current and voltage (I–V) traces were obtained during self-break conditions in a mixture of 1-percent Xe/99-percent H_2. Typical traces for a self-breaking and a laser-triggered spark appear in Fig. 6. The I–V traces look qualitatively the same. Quantitatively, the oscillations that appear in both the current and voltage for self-break have larger amplitudes than those for laser-triggered sparks. The frequencies of the oscillations, though, are nearly the same. Interferograms of self-breaking arcs were also obtained and are discussed at the end of the next section.

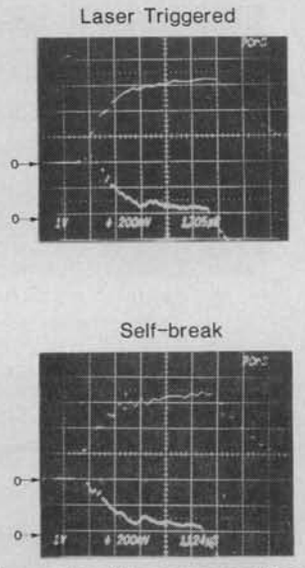

Fig. 6. Voltage and current oscilloscope traces of laser-triggered and self-breaking sparks in 1-percent Xe/99-percent H_2 at 2.0 atm abs. Top trace is current (6.75 kA/div); bottom trace is voltage across the spark gap (8 kV/div); and the time scale is 20 ns/div.

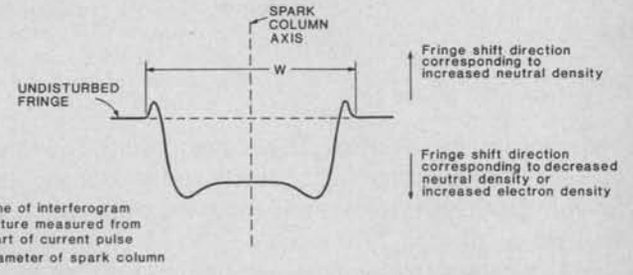

Fig. 7. Schematic of a typical fringe shift pattern from an interferogram.

IV. INTERFEROMETRIC MEASUREMENTS OF THE SPARK COLUMN

To facilitate understanding the interferograms, a schematic drawing of a typical fringe pattern produced by the spark column is shown in Fig. 7. The column pictured is vertically oriented. The interferometer is adjusted to produce upward (or positive) fringe shifts corresponding to increasing gas density. Downward (or negative) fringe shifts correspond to decreasing gas density or increasing electron density. Hence, the net fringe shift is a combined effect of changes in both electron and heavy particle densities. The individual density profiles can be separated by analyzing interferograms taken at two different wavelengths (see Section VI).

A number of different gas mixtures using various mole fractions and pressures of H_2, He, N_2, SF_6, CH_4, Ar, Xe,

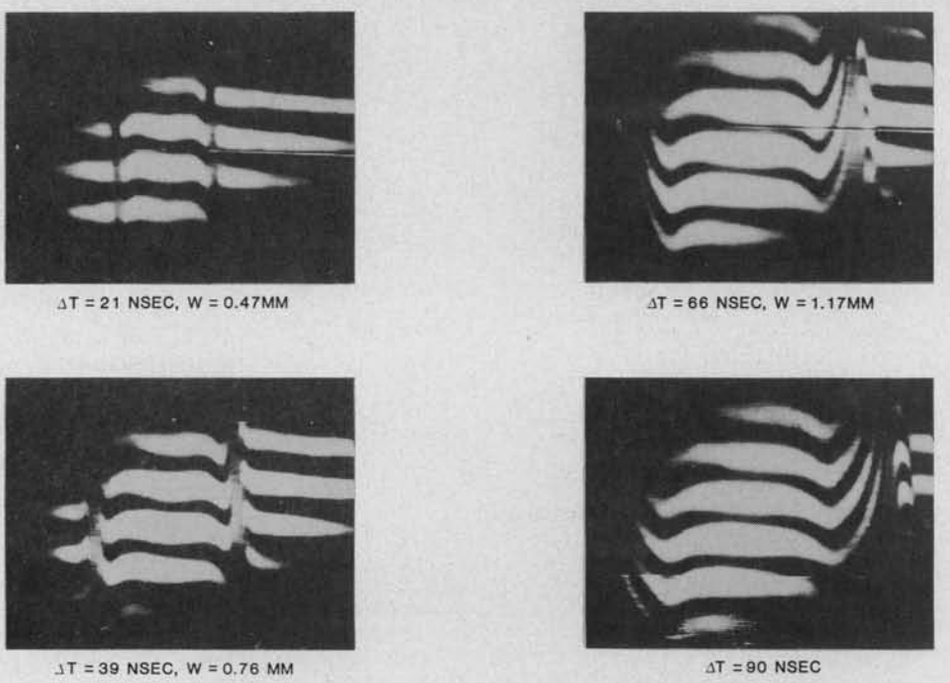

Fig. 8. Temporal evolution of a laser-triggered spark column in 5-percent SF_6/20-percent N_2/75-percent He at 1.5 atm abs. The dye laser wavelength is 392.9 nm, and Δt is the time of the interferogram measured from the start of the current pulse.

and air have been tested. Under appropriate conditions, most of these mixtures can be successfully laser triggered. Sample results for two of these mixtures will be discussed in more detail.

Fig. 8 shows the temporal evolution of the spark column for a 5-percent SF_6/20-percent N_2/75-percent He mixture at 1.5 atm abs. The dye laser is at 392.9 nm, the peak voltage V_{peak} across the spark gap at breakdown is $\approx$ 40 kV ($V_{peak}/V_{SB} \approx 1$), and the peak current after breakdown is $\approx$ 17 kA. The spark column consists of a shell of shocked gas, mostly neutral, at the leading edge surrounding a core of increasing electron density and decreasing neutral density.

Increasing the SF_6 concentration decreases the spark column shell expansion rate. This is because SF_6 is significantly heavier than He and N_2 and therefore has a lower shock speed. Fig. 9 depicts the spark column diameter as a function of time for various SF_6 concentrations. At times less than about 60 ns, the column expansion rate is approximately 8.3×10^5 cm/s at 2.5-percent SF_6 and decreases to approximately 7.2×10^5 cm/s at 10-percent SF_6.

The effect of inadequate preionization on the column formation is demonstrated in Fig. 10. Adequate preionization produces consistent axisymmetric columns as shown in Fig. 10(a). Inadequate preionization tends to produce nonaxisymmetric columns as shown in Fig. 10(b). The difference between the two cases is that the N_2 concentration in Fig. 10(b) is one-half that in Fig. 10(a). It should be noted that in Fig. 10(b), the laser still initiates the spark breakdown; that is, it still has temporal control of the breakdown process. This is in contrast to self-breaking arcs where there is very little temporal or spatial control of the spark breakdown. This temporal and spatial jitter also makes it difficult to obtain meaningful interferograms of self-breaking arcs. Examples of interferograms of self-breaking arcs are given in Fig. 11, for the same switch conditions as in Fig. 6.

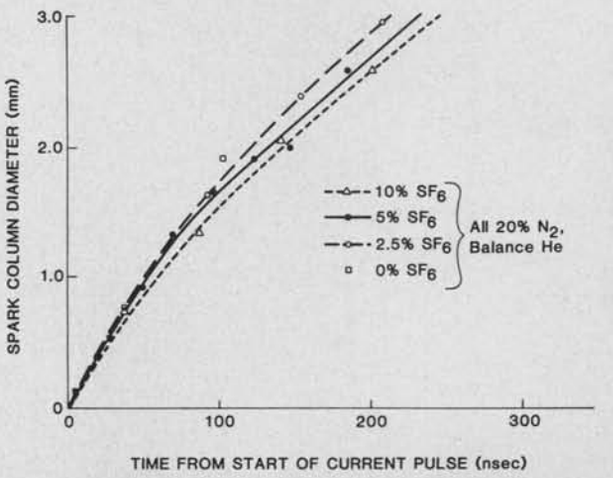

Fig. 9. Dependence of spark column expansion on SF_6 concentration. Pressure is 1.5 atm abs; the electrode spacing is 1.2 cm; the dye laser wavelength is 392.9 nm; $V_{peak} \approx 36$ kV; and $I_{peak} \approx 16$ kA.

For self-breaking sparks, the interferograms fail to show the orderly radial symmetry that appears in laser-triggered sparks. The self-break sparks, though, are nearly vertical in their orientation. Multichanneling was observed in more than half of the interferograms taken under self-break conditions. Streamers were observed to be often present alongside the main arc. For self-breaking sparks

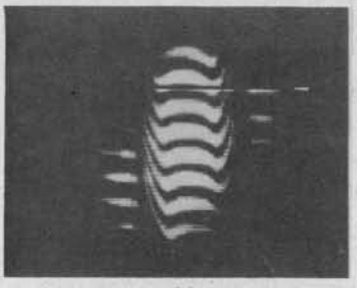

(a)

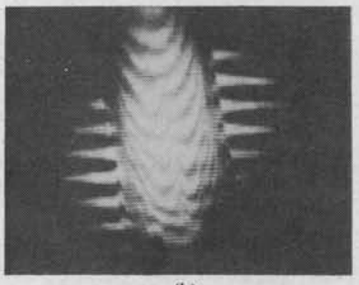

(b)

Fig. 10. Effect of inadequate laser preionization on spark column formation. Adequate laser preionization results in very reproducible axisymmetric spark columns as demonstrated in (a) for a 5-percent SF_6/20-percent N_2/75-percent He gas mixture. Inadequate laser preionization tends to produce nonaxisymmetric columns as shown in (b) for a 5-percent SF_6/10-percent N_2/85-percent He mixture. In both cases the pressure is 1.5 atm abs, and the dye laser wavelength is 392.9 nm.

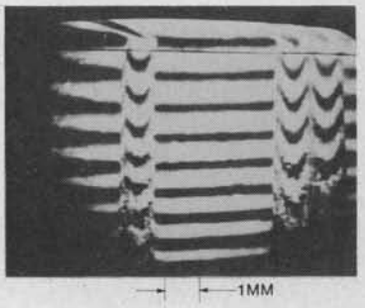

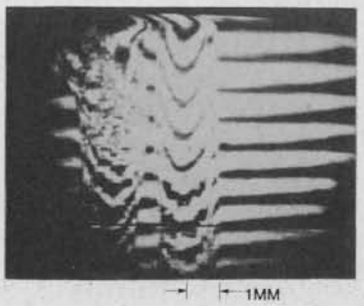

Fig. 11. Examples of interferograms of self-breaking sparks in 1-percent Xe/99-percent H_2 at 2.0 atm abs, and $V_{peak} \approx 30$ kV.

in which only a single channel appears in the interferogram, other channels may be present outside of the field of view. Again, the statistical nature of the self-breakdown process makes it difficult to assign an exact number to the probability of multichanneling. Note also that the self-breaking sparks all show some degree of turbulence. The turbulence appears to start at either end of the spark

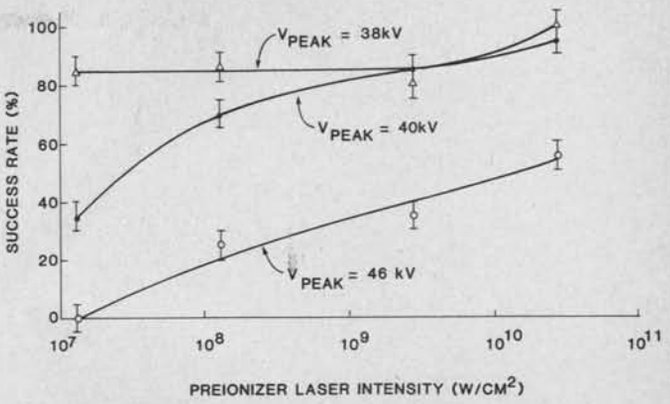

Fig. 12. Laser-triggering success rate for the same conditions as given in Fig. 6. Successful triggering is defined as the formation of an axisymmetric spark channel.

first, and to propagate towards the middle. This observation may be evidence that electric-field distortion near the electrodes or other electrode-induced effects are responsible for the apparent turbulence.

V. Laser-Triggering Dependence on Laser Energy

The minimum preionizer energy necessary to trigger the spark gap was measured to facilitate comparison of our results with other volume preionized laser-triggered switch work. At the focus inside the spark chamber, the preionizer laser delivers approximately 2.8 mJ with a pulsewidth of roughly 10 ns (averaging over the double pulse shown in Fig. 2). The spot size is estimated to be 35 μm in diameter. This implies the peak intensity at the focus is $\approx 2.8 \times 10^{10}$ W/cm^2.

Fig. 12 shows the laser-triggering success rate as a function of the preionizer laser intensity for three different peak voltages (i.e., the voltage just before the onset of voltage collapse). For this measurement, the preionizer beam was attenuated using UV neutral density filters. The success rate is determined by observing the number of well-formed spark columns generated during a sequence of shots. A well-formed column is defined as an axisymmetric spark channel with no evidence of streamer formation inside or outside the column and is temporally controlled by the laser beam. As can be seen in Fig. 12, successful laser triggering is possible over a very wide range in laser intensity. Even at intensities three orders of magnitude below the nominal operating intensity, reasonably dependable laser triggering can be obtained at the lower charge voltages. These results appear to be consistent with the laser energies used by other experiments [12]. At high charge voltages the reliability degrades because self-breakdown begins to compete with laser triggering. The laser-triggering reliability may be even better at charge voltages less than 38 kV; however, this could not be tested due to the minimum triggering limits of the Marx charging system.

With the pulsed self-breakdown data, it is possible to calibrate the relative reliability of laser triggering under the conditions of our experiment. The calibration consists

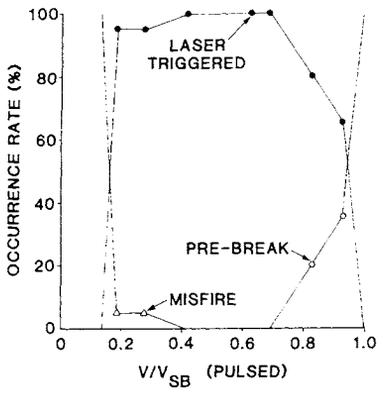

Fig. 13. Reliability of laser triggering pure SF_6. Prebreak is defined as breakdown occurring before arrival of the laser light pulse. Misfire is defined as absence of breakdown occurring after arrival of the laser light pulse. The laser intensity is $\approx 2.8 \times 10^{10}$ W/cm^2.

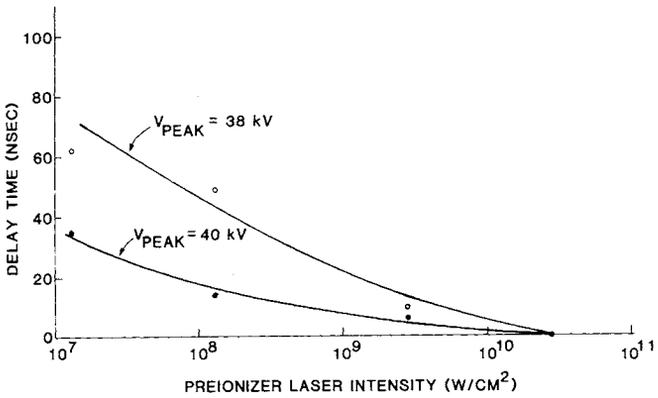

Fig. 14. Delay time between arrival of the preionizer laser beam and spark breakdown (i.e., beginning of current rise) for the data given in Fig. 12.

of laser triggering over a large range of charging voltages many times and keeping account of the number of occurrences of successful laser triggering, prebreaks (i.e., breakdown before the desired charging voltage is reached), and misfires (i.e., unsuccessful laser triggering). The laser triggering was adjusted to occur near the peak of the charge cycle. Hence, the prebreaks are indicative of self-breakdown competing with laser triggering, and misfires are indicative of inadequate preionization to initiate spark formation.

The results for the calibration of pure SF_6 at a laser intensity of $\approx 2.8 \times 10^{10}$ W/cm^2 appear in Fig. 13, plotted as a function of the ratio $F_{SB} = V/V_{SB}$ (pulsed). For $0.35 < F_{SB} < 0.75$, laser triggering can be obtained with virtually 100-percent reliability. Below this range, misfires account for approximately 5 percent of all trials. Above this range, prebreak becomes progressively more dominant.

Fig. 14 gives the delay time between the arrival of the preionizer laser beam and the onset of spark breakdown (i.e., the beginning of the rise in the current pulse) as a function of the preionizer laser intensity. The accuracy of these measurements is ± 5 ns. The measurements demonstrate that at one-tenth the nominal operating intensity, the delay time is less than 10 ns.

VI. Interpretation of Data

One of the advantages of laser interferometry with respect to studying spark column formation is the ability to obtain detailed and absolute measurements of the electron and heavy particle density profiles within the arc channel. This is possible because the electrons and heavy particles affect the fringe pattern in opposing and well-understood manners. For example, in the 5-percent SF_6/20-percent N_2/75-percent He mixture at 1.5 atm, the refractive index for each of the constituent gases is 1.0011, 1.00030, and 1.000036, respectively. There is negligible dependence on wavelength over the range of interest in this work. For our experimental conditions, the fringe shift Δm due to change in the gas density $\Delta\rho$ from ambient ρ_0 over a length l in the optical path at wavelength λ is given by

$$\Delta m = 0.00021(\Delta\rho/\rho_0)\,(l/\lambda). \tag{1}$$

It is seen that the shorter the wavelength, the larger the fringe shift. For free electrons, the fringe shift, obtained from the index of refraction as calculated from the plasma dispersion relation, is

$$\Delta m = -4.48 \times 10^{-14} n_e \lambda l. \tag{2}$$

Note that the fringe shift is in the opposite direction to that of the heavy particles, and increases with increasing wavelength. This analysis assumes there are no excited atomic states with transitions near the measurement wavelengths that contribute significantly to the refractive index. This assumption was validated for the wavelengths used during this experiment by streak camera spectroscopy of representative gas mixtures. Since the fringe shifts caused by the electrons and heavy particles have opposite wavelength dependences, it is possible to separate their contribution to the total fringe pattern by obtaining interferograms at the same time during the arc but at two different wavelengths.

Reduction of the fringe data to obtain the heavy particle and electron profiles begins by digitizing the fringe pattern of the interferogram. A computer program performs an Abel inversion [13] of the digitized data. This process is described in more detail in the Appendix.

Using (1) and (2), the fringe shift as a function of radius $\Delta m(r)$ for two different wavelengths λ_1 and λ_2 is then given by

$$\Delta m_1(r) = \frac{a}{\lambda_1}\Delta N(r) - b\lambda_1 n_e(r) \tag{3}$$

$$\Delta m_2(r) = \frac{a}{\lambda_2}\Delta N(r) - b\lambda_2 n_e(r) \tag{4}$$

where a and b are constants, ΔN is the change in the heavy particle density, and n_e is the electron density. By taking data at two different wavelengths, (3) and (4) can be solved simultaneously for $n_e(r)$ and $\Delta N(r)$. In solving these equations, self-consistency is checked by requiring a conservation of mass; that is

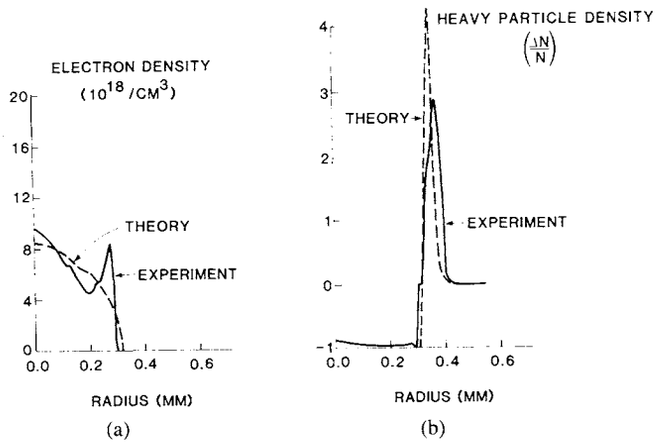

Fig. 15. Comparison of experimental and theoretical density profiles for the case given in Fig. 18.

$$\int_0^\infty \Delta N(r) r \, dr = 0.$$

The calculated profiles of n_e and ΔN, for the fringe pattern appearing in the Appendix (see Fig. 18), are shown in Fig. 15. The electron density reaches a maximum of nearly 10^{19} cm^{-3}. The shocked gas forms a shell outside the interior column of high electron density and is rarefied within the column. Superimposed on the experimental curves in Fig. 15 are the predictions from the theoretical computer model for the same experimental conditions. The computer code is discussed in more detail in [7].

There is a significant uncertainty as to the size of the local maximum in electron density just interior to the heavy particle shell of the experimental data. This uncertainty is caused by an uncertainty associated with the normalization of the experimental data taken at the two different wavelengths. Although the data are normalized to the shock fronts, the uncertainty in the exact location of the front and in the delay time of each interferogram will change the magnitude of the electron shell calculated. For the case given in Fig. 15(a), we estimate that the peak of the electron shell may vary between at most 4×10^{18} cm^3 and 12×10^{18} cm^3. However, the rest of the electron profile has an uncertainty of only ± 10 percent.

The average electron density as derived from the interferograms is plotted as a function of time in Fig. 16 for various breakdown voltages in 1-percent Xe/99-percent H_2 and for 5-percent SF_6/20-percent N_2/75-percent He at $V_{peak} \approx 40$ kV. Also shown is the prediction from the model.

A study of the effects of high plasma density on the expressions for refractive index due to free electrons was performed. This study was conducted because the electron densities measured during this experiment are under certain conditions very high ($\geq 10^{19}$ cm^{-3}) and there was a need to confirm the validity of the expressions used in the analysis of the data at these high electron densities.

There is a reduction in the refractive effect of free electrons due to collisions, if the collision frequency approaches the frequency of the light, according to the expression

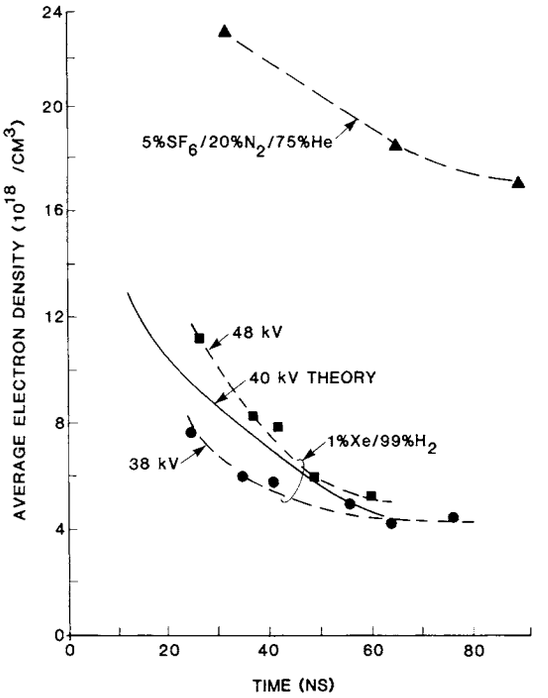

Fig. 16. Average spark column electron densities as a function of time. The 5-percent SF_6/20-percent N_2/75-percent He mixture is for a breakdown voltage of ≈ 40 kV; the breakdown voltages for the 1-percent Xe/99-percent H_2 are shown in the figure. The solid curve is the prediction based on our computer model.

$$n = 1 - \frac{n_e/n_c}{2(1 + \nu_c^2/\omega^2)}$$

where n_e is the electron density, ω is the frequency of the light (in radians per second), n_c is the critical density at ω, and ν_c is the collision frequency. For our observed plasma parameters (2×10^{19} electron/cm^3) and diagnostic wavelength (≈ 600 nm), $\nu_c/\omega < 0.1$ and this particular correction to the refractive index is less than 1 percent.

Another plasma effect that may change the index of refraction is the generation of significant density perturbations caused by plasma microinstabilities. This concern arises because the spark column current density is very high ($> 10^6$ A/cm^2), and the electron drift velocity is comparable with the ion thermal speed. These plasma conditions could lead to an ion-acoustic instability [14] or a streaming instability, although the highly collisional nature of the spark plasma may dampen the growth of microinstabilities. The resulting density perturbations, if present, would have their k vector parallel to the current flow, and the effect on visible light would depend on the orientation of the polarization vector relative to the spark column axis.

Interferograms were taken with the dye laser beam polarized parallel, perpendicular, and unpolarized (normal operation) with respect to the axis of the spark column. The fringe patterns were identical for all three cases. This result suggests that plasma instabilities, if present, do not significantly alter the refractive index of the plasma.

VII. Conclusion

The simultaneous usage of laser triggering and laser interferometry has been utilized as a diagnostic tool for studying spark columns. Reproducible and axisymmetric spark columns as well as precise temporal and spatial control of the spark breakdown are obtained when using laser triggering; both of these are necessary for accurate short-pulse interferometry measurements. The tunable dye laser interferometer system yielded high temporal and spatial resolution interferograms of the spark column from which information concerning the electron and neutral densities was obtained.

Appendix
Details of Abel Inversion Process

This section explains in more detail how the line-of-sight data of the spark column which is recorded by the interferogram are Abel inverted in order to obtain the true radial dependence of the observed fringe shifts.

The fringe patterns are converted into a numeric computer file using a Talos Systems digitizer. Uncertainties associated with the digitizing are primarily caused by the finite thickness of the fringes. Some of this thickness is the result of fringe movement during the 5-ns dye laser pulse.

A computer program performs an Abel inversion [13] of the digitized data. In doing this, the program first fits the data to a polynomial, $F_j(x)$, over N subregions of the fringe pattern, as shown schematically in Fig. 17. (Note, the fringe pattern in Fig. 17 is inverted and one-half of the pattern depicted in Fig. 7.) Each polynomial is described by

$$F_j(x) = \sum_{k=1}^{m} a_{jk} x^k, \qquad (j = 1, N)$$

where a_{jk} are coefficients determined by a least-mean-square error curve fit to the data; x is transverse distance measured from the center of the column; and m is the order of the polynomial. The order is preselected and is typically 2 or 3, with a maximum allowed value of 9. Curve smoothing of the original data reduces the errors during the Abel inversion process caused by noise in the digitization process and by the need to numerically differentiate the data. The data are normalized to the shock fronts to reduce uncertainties in the timing of separate interferograms and inverted using the polynomial curve. The inverted data $G(r)$ as a function of the column radius r are given by

$$G(r) = -\frac{1}{\pi} \sum_{j=1}^{N} \int_{x_j}^{x_{j+1}} \frac{\theta(x, r)}{(x^2 - r^2)^{1/2}} \sum_{k=1}^{m} k a_{jk} x^{k-1}\, dx,$$

$$\theta(x, r) = \begin{cases} 1, & x > r \\ 0, & x < r \end{cases}.$$

Typical results of this inversion are shown in Fig. 18 for a 1-percent Xe/99-percent H_2 mixture. The interferogram is shown in Fig. 18(a). The digitized fringe patterns for this mixture at two different wavelengths are shown in Fig. 18(b). For both patterns $\Delta t = 45$ ns, $V_{peak} \approx 40$ kV ($V_{peak}/V_{SB} \approx 1$), and $P = 2.0$ atm abs. Note, the digitized patterns are inverted with respect to the fringe pattern shown in Fig. 18(a). Fig. 18(c) shows the inverted data; the uncertainty in the inversion at the center of the column, as indicated by the dotted lines, is due to termination errors in the Abel inversion process.

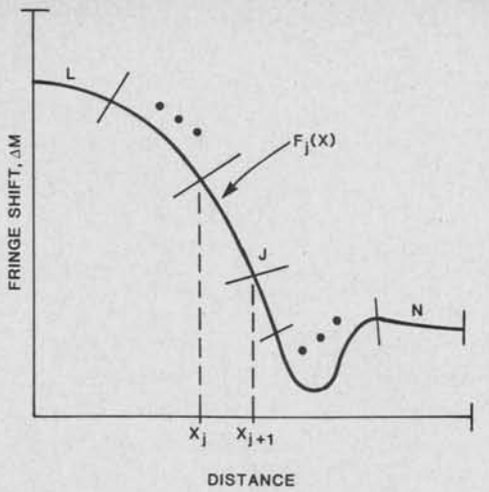

Fig. 17. Schematic of one-half of a typical fringe shift pattern showing how sections of the pattern are curve-fitted to polynomials $F_j(x)$ as part of the Abel inversion process.

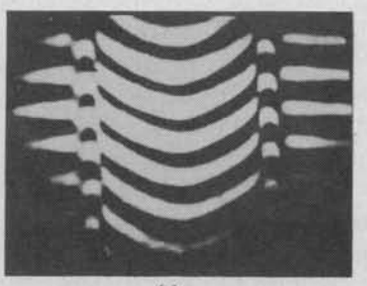

(a)

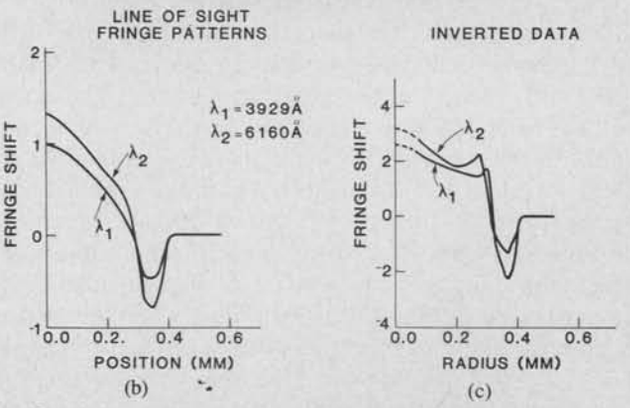

(b) (c)

Fig. 18. Abel inversion of a spark column fringe pattern. Gas mixture: 1-percent Xe/99-percent H_2; $\Delta t = 45$ ns; $V_{peak} \approx 40$ kV; and $P = 2.0$ atm abs. (a) Original interferogram taken at 392.9 nm. (b) Digitized fringe patterns at two different wavelengths (note that the digitized patterns are inverted with respect to the pattern in (a)). (c) Abel inverted data.

Acknowledgment

The authors wish to thank Dr. R. J. Gripshover, Dr. E. D. Ball, and Dr. D. B. Fenneman at the Naval Surface

Weapons Center for their helpful input during this experiment. They would like to acknowledge D. M. Barrett, who was responsible for the design and testing of the Marx bank system, and J. F. Seamans and D. H. Ford for their assistance during the experiments.

REFERENCES

[1] J. R. Woodworth, R. G. Adams, and C. A. Frost, "UV-laser triggering of 2.8-megavolt gas switches," *IEEE Trans. Plasma Sci.*, vol. PS-10, pp. 257-261, 1982.

[2] J. Bailey, Y. Ettinger, A. Fisher, and N. Rostoker, "Gas-puff Z pinches with D_2 and D_2-Ar mixtures," *Appl. Phys. Lett.*, vol. 40, pp. 460-462, 1982.

[3] L. D. Horton and R. M. Gilgenbach, "Collinear investigation of laser initiated reduced density channels," *Appl. Phys. Lett.*, vol. 43, pp. 1010-1012, 1983.

[4] A. H. Guenther and J. R. Bettis, "The laser triggering of high-voltage switches," *J. Phys. D: Appl. Phys.*, vol. 11, pp. 1577-1613, 1978.

[5] R. A. Dougal and P. F. Williams, "Fundamental processes in laser-triggered electrical breakdown in gases," *J. Phys. D: Appl. Phys.*, vol. 17, pp. 903-918, 1984.

[6] S. K. Dahli and P. F. Williams, "Numerical simulation of streamer propagation in nitrogen at atmospheric pressures," *Phys. Rev. A*, vol. 31, pp. 1219-1221, 1985.

[7] M. J. Kushner, R. D. Milroy, and W. D. Kimura, "A laser triggered spark gap model," *J. Appl. Phys.*, vol. 58, pp. 2988-3000, 1985.

[8] W. D. Kimura, E. A. Crawford, M. J. Kushner, and S. R. Byron, "Investigation of laser preionization triggered high power switches using interferometric techniques," in *Proc. 16th Power Modulator Symp.* (Arlington, VA), June 18-20, 1984, IEEE pub. 84 CH2056-0, pp. 54-63, 1984.

[9] W. D. Kimura, M. J. Kushner, D. H. Ford, and S. R. Byron, "Dual channel formation in a laser triggered spark gap," *J. Appl. Phys.*, vol. 58, pp. 4015-4023, 1985.

[10] D. M. Barrett *et al.*, "A low inductance capacitive probe for spark gap voltage measurements," *Rev. Sci. Instr.*, vol. 56, pp. 2111-2115, 1985.

[11] M. J. Kushner, W. D. Kimura, and S. R. Byron, "Arc resistance of laser-triggered spark gaps," *J. Appl. Phys.*, vol. 58, pp. 1744-1751, 1985.

[12] W. R. Rapoport, J. Goldhar, and J. R. Murray, "KrF laser-triggered SF_6 spark gap for low jitter timing," *IEEE Trans. Plasma Sci.*, vol. PS-8, pp. 167-170, 1980.

[13] W. L. Barr, "Method for computing the radial distribution of emitters in a cylindrical source," *J. Opt. Soc. Amer.*, vol. 52, pp. 885-888, 1962.

[14] D. B. Fenneman, M. Raether, and M. Yamada, "Ion-acoustic instability in the positive column of a helium discharge," *Phys. Fluids*, vol. 16, pp. 871-878, 1973.